Available online at www.sciencedirect.com
ScienceDirect
Journal of Power Sources 160 (2006) 1122–1130
JOURNAL OF POWER SOURCES
www.elsevier.com/locate/jpowsour

Predictions of phase temperatures in a porous cathode of polymer electrolyte fuel cells using a two-equation model

C.H. Chao [a,*], Azai J.J. Hwang [b]

[a] *Department of Electrical Engineering, Ta-Hua Institute of Technology, Hsinchu County 307, Taiwan*
[b] *Institute of Material and System Engineering, MingDao University, Changhua County 523, Taiwan*

Received 10 December 2005; received in revised form 1 March 2006; accepted 3 March 2006
Available online 19 May 2006

Abstract

In this study, both solid-phase and fluid-phase temperatures inside a porous cathode of a polymer electrolyte fuel cell in contact with an interdigitated gas distributor are predicted numerically. The porous cathode consists of a catalyst layer and a diffusion layer. The heat transfer in the catalyst layer is coupled with species transports via a macroscopic electrochemical model. On the other hand, in the diffusion layer, the energy equations based on the local thermal non-equilibrium (LTNE) are derived to resolve the temperature difference between the solid phase and the fluid phase. As for the species transports, the Bruggemann model is employed to describe the effective diffusivities of the oxygen and water vapor in the porous cathode. Results show that the wall temperature decreases with increasing the intrinsic heat transfer coefficient. As the intrinsic heat transfer coefficients increase, the porous electrode becomes local thermal equilibrium with a strong thermal interaction (heat transfer) between the solid and fluid phases. Under the conditions of high intrinsic heat transfer coefficients, the temperature difference between the solid matrices and the reactant fluids are negligible.

Keywords: Porous cathode; Polymer electrolyte fuel cell; Catalyst layer; Diffusion layer; Local thermal non-equilibrium (LTNE)

1. Introduction

Thermal transports in a polymer electrolyte fuel cell (PEFC) have received a particular attention due to their strong effect on the fuel cell durability. The electrode of a PEFC is a typical porous medium. In this medium, the heat dissipation by the electrochemical reaction in the active layer of a fuel cell should be removed thoroughly to sustain proper operation.

There are two tasks in the thermal management of a low-temperature fuel cell. The first is to optimize the operating temperature range that avoids the local hot spot as well as the water flooding. The second task is to keep a uniform temperature distribution that avoids the thermal stress in the porous electrode. Therefore, a superior thermal management becomes critical for safely operating and prolonging a fuel cell.

However, most investigations about the porous electrode of a fuel cell did not consider thermal transports [1–5] and only a few discussed the thermal behaviours in the porous electrode based on the local thermal equilibrium (LTE) assumption [6–9]. The LTE approach is simple and straightforward but is only applicable if the temperature difference between the solid and the fluid phases is very small. The so-called one-equation model is employed to resolve the phase-mixing temperatures in the porous medium. When the temperature difference is significant, it becomes a local thermal non-equilibrium (LTNE). The one-equation model is invalid, and should be modified with the two-equation model, which treats the solid-phase temperature and the fluid-phase temperature separately. An analysis of heat transfer in a porous medium based on the two-equation model is more involved because it requires interstitial information inside the porous medium such as heat transfer coefficient between the fluid and solid phases and the interfacial surface area [10–12]. Due to this difficulty, most investigations about the porous electrode of a fuel cell resorted to using the one-equation model to obtain the phase-mixing temperatures.

Studies discussing the phase-temperature difference between the reactant fluids and the solid matrices inside the porous electrode of a polymer electrolyte fuel cell are rather sparse [13,14],

* Corresponding author. Tel.: +886 35507641; fax: +886 422518272.
E-mail address: rjhome@ms4.kntech.com.tw (C.H. Chao).

0378-7753/$ – see front matter © 2006 Elsevier B.V. All rights reserved.
doi:10.1016/j.jpowsour.2006.03.010

Nomenclature

Bi	Biot number
c_{H_2O}	water vapor mole concentration (mol m^{-3})
$c_{H_2O,ref}$	water vapor mole concentration at inlet (mol m^{-3})
C_{H_2O}	normalized water vapor concentration, c_{H_2O}/c_{tot}
$C_{H_2O,ref}$	normalized water vapor mole concentration at inlet, $c_{H_2O,ref}/c_{tot}$
c_{O_2}	oxygen concentration (mol m^{-3})
$c_{O_2,ref}$	oxygen mole concentration at inlet (mol m^{-3})
C_{O_2}	normalized oxygen concentration, c_{O_2}/c_{tot}
$C_{O_2,ref}$	normalized oxygen mole concentration at inlet, $c_{O_2,ref}/c_{tot}$
c_p	specific heat at constant temperature (J kg^{-1} K^{-1})
c_{tot}	total mole concentration of the reacting fluid (mol m^{-3})
d	pore diameter of the porous medium (m)
D_{H_2O}	binary diffusivity of water vapor in the oxygen (m^2 s^{-1})
$D_{H_2O,eff}$	effective diffusivity of water vapor in the gas diffusion layer (m^2 s^{-1})
D_{O_2}	binary diffusivity of oxygen in the water vapor (m^2 s^{-1})
$D_{O_2,eff}$	effective diffusivity of oxygen in the gas diffusion layer (m^2 s^{-1})
Da	Darcy number
Ec_1, Ec_2	coefficients in Eq. (23)
F	Faraday's constant (96487 C mol^{-1})
h_V	interstitial heat transfer coefficient in the porous medium (W m^{-3} K^{-1})
I	current (A)
k	thermal conductivity (W m^{-1} K^{-1})
L	length of the computational domain, 160 μm (m)
$\dot{m}$	mass flux (kg m^{-2} s^{-1})
p	pressure (Pa)
P	non-dimensional pressure
Pr	Prandtl number
Q	heat dissipation by the electrochemical reaction (W)
Re	Reynolds number
R_{M1}, R_{M2}	coefficients in Eq. (24)
R_{N1}, R_{N2}	coefficients in Eq. (25)
R_Ω	ohmic resistance (Ω)
S_V	surface area-to-volume ratio (m^{-1})
Sc	Schmidt number
St	Stanton number
T	temperature (K)
u, v	velocity components in the x, and y directions, respectively (m s^{-1})
U, V	non-dimensional velocity components in the x, and y directions
W	channel width, 40 μm
W_s	shoulder width, 80 μm
x, y	coordinate system (m)
X, Y	non-dimensional x and y coordinate

Greek symbols

α_1, α_2	coefficients in Eq. (11)
δ	thickness of the diffusion layer, 40 μm (m)
δ_c	thickness of the catalyst layer, 10 μm (m)
ε	porosity of the diffusion layer
ε_C	porosity of the catalyst layer
η	cathodic overpotential (V)
θ	non-dimensional temperature
κ	permeability (m^2)
ρ	density (kg m^{-3})
τ	tortuosity

and this has motivated the present research to develop a two-equation model to predict the fluid and solid temperatures inside the porous electrode of a polymer electrolyte fuel cell. The effects of the intrinsic heat transfer coefficient of the porous electrode on the heat/mass transfer mechanisms are examined and, as a result, thermal paths in a porous cathode of polymer electrolyte fuel cell are clearly identified. It would be of assistance for further accurate analyses of the fuel-cell thermal performance by considering the thermally dependent physical properties inside a polymer electrolyte fuel cell.

2. Numerical model

Fig. 1(a) shows a sectional view of a porous cathode in contact with an interdigitated flow field of a polymer electrolyte fuel cell. The present computational module is limited in the module shown in Fig. 1(b). The oxygen reduction reaction (ORR) on the cathode is considered in the present model.

$$O_{2(g)} + 4H^+ + 4e^- \leftrightarrow 2H_2O_{(g)} \quad (1)$$

The oxygen–water vapour mixture enters the porous cathode form the module inlet (inlet channel), and then transverses the diffusion layer to the catalyst layer. The electrochemical reaction occurring in the catalyst layer consumes the oxygen (C_{O_2}) and, meanwhile, produces the water vapour (C_{H_2O}). In addition, the heat (Q) is generated by the overpotential and irreversibility during the electrochemical reaction. Either the fluid or the solid removes it. The assumptions in this model include: (i) mixtures are ideal gas; (ii) flow is steady, laminar, and incompressible; (iii) thermal physical properties are constant; (iv) porous electrode is homogeneous and isotropic; (v) water exits as vapour only and (vi) both inlet-fluid temperature and rib-surface temperature are uniform.

2.1. Governing equations

In the porous layers, the steady volume-averaged continuity and momentum equations that govern fluid flow are given by

$$\frac{\partial(\rho_f u)}{\partial x} + \frac{\partial(\rho_f v)}{\partial y} = S_c \quad (2)$$

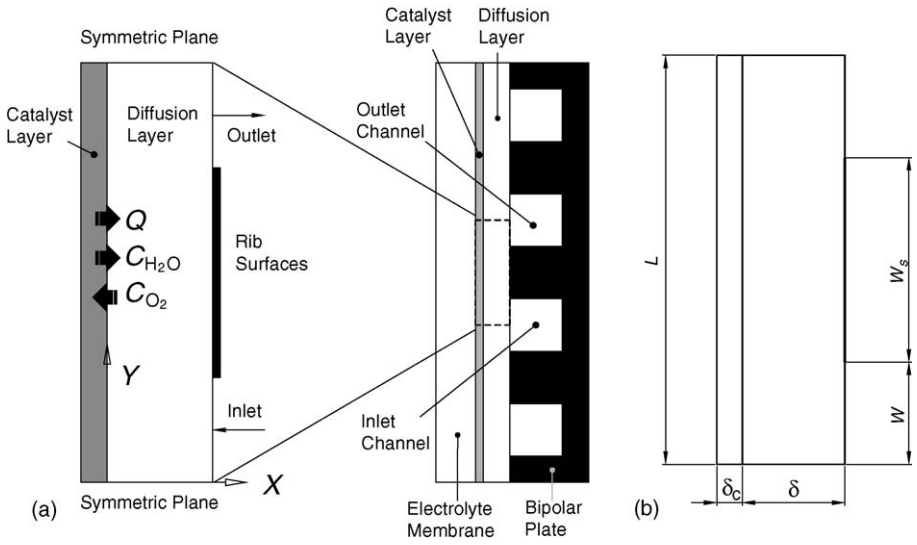

Fig. 1. (a) Schematic drawing of porous electrode of the interdigitated flow field. (b) Configuration of the computational domain.

$$\rho_f u\frac{\partial u}{\partial x}+\rho_f v\frac{\partial u}{\partial y}=-\frac{\partial p}{\partial x}+\mu\left(\frac{\partial^2 u}{\partial x^2}+\frac{\partial^2 u}{\partial y^2}\right)+S_u \tag{3}$$

$$\rho_f u\frac{\partial v}{\partial x}+\rho_f v\frac{\partial v}{\partial y}=-\frac{\partial p}{\partial y}+\mu\left(\frac{\partial^2 v}{\partial x^2}+\frac{\partial^2 v}{\partial y^2}\right)+S_v \tag{4}$$

The source terms in Eqs. (3) and (4) relate to the traditional Darcy dissipation. It is used to account for the pressure drop due to viscous friction at the surfaces of carbon fibbers, i.e., $S_u=-\varepsilon\mu u/\kappa$ and $S_v=-\varepsilon\mu v/\kappa$, respectively. As for the energy equations, the two-equation model is used to describe the thermal behaviour in the diffusion layer [12]. The energy equations for solid and fluid phases, respectively, are:

$$0=k_{s,\mathrm{eff}}\left(\frac{\partial^2 T_s}{\partial x^2}+\frac{\partial^2 T_s}{\partial y^2}\right)-h_V(T_s-T_f)-\frac{i_s^2}{\sigma_{s,\mathrm{eff}}} \tag{5}$$

$$(\rho c_p)_f u\frac{\partial T_f}{\partial x}+(\rho c_p)_f v\frac{\partial T_f}{\partial y}=k_{f,\mathrm{eff}}\left(\frac{\partial^2 T_f}{\partial x^2}+\frac{\partial^2 T_f}{\partial y^2}\right)+h_V(T_s-T_f) \tag{6}$$

The last two terms of Eq. (5) mean the convective heat delivered to the reactant fluids from the carbon fibers and the Joule-heating effect, respectively. The last term of Eq. (6) represents the heat received by the reactant fluids from the carbon fibers.

The effective thermal conductivities for the solid phase and the fluid phase are respectively defined as

$$k_{s,\mathrm{eff}}=(1-\varepsilon)k_s \tag{7}$$

$$k_{f,\mathrm{eff}}=\varepsilon k_f \tag{8}$$

In the catalyst layer, physically, the electrochemical reaction occurs at the interface of reactant (fluid) and catalyst (solid) under a fixed temperature. Therefore, the fluid and solid phases in the catalyst layer have the same local temperatures, i.e.,

$$T_f=T_s \tag{9}$$

$$(\rho c_p)_f u\frac{\partial T_f}{\partial x}+(\rho c_p)_f v\frac{\partial T_f}{\partial y}=k_{c,\mathrm{eff}}\left(\frac{\partial^2 T_f}{\partial x^2}+\frac{\partial^2 T_f}{\partial y^2}\right)+j_T\eta \tag{10}$$

The source term $j_T\eta$ represents the overpotential heating by the electrochemical reaction. According to the Butler-Volmer correlation [15], the relationship between the local transfer current density and the reactant concentrations can be described as the following equation.

$$j_T=\alpha_1\left(\frac{c_{O_2}}{c_{O_2,\mathrm{ref}}}\right)-\alpha_2\left(\frac{c_{H_2O}}{c_{H_2O,\mathrm{ref}}}\right)^2 \tag{11}$$

α_1 and α_2 are electrochemical coefficients depending on the exchange current density, the overpotential on the electrode surfaces, and the reacting temperature. It is known that the kinetics of oxygen reduction reaction is related to the temperature. Since the temperature variation in reacting layer for the PEFC is small, the temperature effect on the kinetics of ORR is negligible. Consequently, the coefficients α_1 and α_2 are regarded as constants in the present model.

The species transports of the oxygen and water vapor in the porous cathode can be governed by the following equations:

$$u\frac{\partial c_{O_2}}{\partial x}+v\frac{\partial c_{O_2}}{\partial y}=D_{O_2,\mathrm{eff}}\left(\frac{\partial^2 c_{O_2}}{\partial x^2}+\frac{\partial^2 c_{O_2}}{\partial y^2}\right)+S_{O_2} \tag{12}$$

$$u\frac{\partial c_{H_2O}}{\partial x}+v\frac{\partial c_{H_2O}}{\partial y}=D_{H_2O,\mathrm{eff}}\left(\frac{\partial^2 c_{H_2O}}{\partial x^2}+\frac{\partial^2 c_{H_2O}}{\partial y^2}\right)+S_{H_2O} \tag{13}$$

In the catalyst layer, the sources terms for oxygen transport and water-vapor transport are $S_{O_2}=j_T/4F$ and $S_{H_2O}=-j_T/2F$, respectively. In the diffusion layer, they are 0. The effective diffusivities of the oxygen and water vapour in the porous electrode, $D_{O_2,\mathrm{eff}}$ and $D_{H_2O,\mathrm{eff}}$, follows the Bruggemann model [16], i.e.,

$$D_{O_2,\mathrm{eff}}=\varepsilon^\tau D_{O_2} \tag{14}$$

Table 1
Governing equations of the present model

	Equations	S_Φ	
		Diffusion layer	Catalyst layer
Mass	$\frac{\partial U}{\partial X}+\frac{\partial V}{\partial Y}=S_\Phi$	0	S_Φ
Momentum	$U\frac{\partial U}{\partial X}+V\frac{\partial U}{\partial Y}=-\frac{\partial P}{\partial X}+\frac{1}{Re}\left(\frac{\partial^2 U}{\partial X^2}+\frac{\partial^2 U}{\partial Y^2}\right)+S_\Phi$	$-\frac{1}{ReDa}\varepsilon U$	$-\frac{1}{ReDa}\varepsilon_C U$
	$U\frac{\partial V}{\partial X}+V\frac{\partial V}{\partial Y}=-\frac{\partial P}{\partial Y}+\frac{1}{Re}\left(\frac{\partial^2 V}{\partial X^2}+\frac{\partial^2 V}{\partial Y^2}\right)+S_\Phi$	$-\frac{1}{ReDa}\varepsilon V$	$-\frac{1}{ReDa}\varepsilon_C V$
Energy, diffusion layer	$0=\frac{\partial^2\theta_s}{\partial X^2}+\frac{\partial^2\theta_s}{\partial Y^2}+S_\Phi$	$Bi(\theta_f-\theta_s)$	–
	$U\frac{\partial\theta_f}{\partial X}+V\frac{\partial\theta_f}{\partial Y}=\frac{1}{RePr_{eff}}\left(\frac{\partial^2\theta_f}{\partial X^2}+\frac{\partial^2\theta_f}{\partial Y^2}\right)+S_\Phi$	$St(\theta_s-\theta_f)$	–
Energy, catalyst layer	$\theta_s=\theta_f$	–	–
	$U\frac{\partial\theta_f}{\partial X}+V\frac{\partial\theta_f}{\partial Y}=\frac{1}{RePr_{eff}}\left(\frac{\partial^2\theta_f}{\partial X^2}+\frac{\partial^2\theta_f}{\partial Y^2}\right)+S_\Phi$	–	$\frac{1}{RePr_{eff}}[Ec_1C_{O_2}-Ec_2(C_{H_2O})^2]$
Species	$U\frac{\partial C_{O_2}}{\partial X}+V\frac{\partial C_{O_2}}{\partial Y}=\frac{1}{ReSc_{O_2}}\left(\frac{\partial^2 C_{O_2}}{\partial X^2}+\frac{\partial^2 C_{O_2}}{\partial Y^2}\right)+S_\Phi$	0	$\frac{1}{ReSc_{O_2}}[R_{M1}C_{O_2}-R_{M2}(C_{H_2O})^2]$
	$U\frac{\partial C_{H_2O}}{\partial X}+V\frac{\partial C_{H_2O}}{\partial Y}=\frac{1}{ReSc_{H_2O}}\left(\frac{\partial^2 C_{H_2O}}{\partial X^2}+\frac{\partial^2 C_{H_2O}}{\partial Y^2}\right)+S_\Phi$	0	$\frac{1}{ReSc_{H_2O}}[R_{N1}C_{O_2}-R_{N2}(C_{H_2O})^2]$
Non-dimensional parameters	$X=\frac{x}{\delta}$, $Y=\frac{y}{\delta}$, $u_d=\frac{\dot m}{\rho_f A\varepsilon}$, $U=\frac{u}{u_d}$, $V=\frac{v}{u_d}$, $P=\frac{p}{\rho_f u_d^2}$, $C_{O_2}=\frac{c_{O_2}}{c_{tot}}$,		
	$C_{O_2,ref}=\frac{c_{O_2,ref}}{c_{tot}}$, $C_{H_2O}=\frac{c_{H_2O}}{c_{tot}}$, $C_{H_2O,ref}=\frac{c_{H_2O,ref}}{c_{tot}}$, $\theta=\frac{T-T_r}{T_{f,in}-T_r}$, $Re=\frac{u_d\delta}{\nu}$,		
	$Pr_{eff}=\frac{\mu(c_p)_f}{k_{f,eff}}$, $Bi=\frac{h_s S_V\delta^2}{k_{s,eff}}$, $St=\frac{h_s S_V\delta}{(\rho c_p)_f u_d}$, $Sc_{O_2}=\frac{\nu}{D_{O_2,eff}}$, $Sc_{H_2O}=\frac{\nu}{D_{H_2O,eff}}$,		
	$R_{M1}=\frac{\alpha_1\delta^2}{4Fc_{tot}D_{O_2,eff}}$, $R_{M2}=\frac{\alpha_2\delta^2}{4Fc_{tot}D_{O_2,eff}}$, $Da=\frac{\kappa}{\delta^2}$, $R_{N1}=\frac{\alpha_1\delta^2}{2Fc_{tot}D_{H_2O,eff}}$,		
	$R_{N2}=\frac{\alpha_2\delta^2}{2Fc_{tot}D_{H_2O,eff}}$, $R_k=\frac{k_{f,eff}}{k_{s,eff}}$, $Ec_1=\frac{\alpha_1\eta\delta^2}{k_{s,eff}(T_{f,in}-T_r)C_{O_2,ref}}$, $Ec_2=\frac{\alpha_2\eta\delta^2}{k_{s,eff}(T_{f,in}-T_r)C^2_{H_2O,ref}}$		

Table 2
Porous electrode data sheet

Property name		
Physical properties[a]	Material	Carbon fiber
	Bulk density, ρ	1100 kg m^{-3}
	Specific resistance, σ^{-1}	115 μΩ m
	Thermal conductivity, k	1.71 W m^{-1} K^{-1}[b]
Geometric properties	Diffusion layer porosity, ε	48%
	Catalyst layer porosity, ε_C	42%
	Diffusion layer thickness, δ	400 μm
	Catalyst layer thickness, δ_C	100 μm
	Diffusion layer tortuosity, τ	1.5
	Catalyst layer tortuosity, τ	1.5
	Average pore diameter, d	33 μm
	Diffusion layer permeability, κ[c]	1.57×10^{-12} m^2
	Catalyst layer permeability, κ_C[c]	1.02×10^{-12} m^2
Flow properties	Interstitial heat transfer coefficient, h_V	1.0×10^3 to 1.0×10^9 W m^{-3} (assumed)
	Surface-to-volume ratio, S_V	1.0×10^3 m^{-1} (assumed)
	Pore velocity, u_d for $I=2.0$ A at stoichiometric flow ratio 5	0.478 m s^{-1}

[a] Data from manufacture (Toray).
[b] Oxygen at 25 °C with 15% RH; $p=0.15$ atm; plate thickness, 2.5 cm; 51 L m^{-2} s^{-1}.
[c] ASTM E1530.

$$D_{H_2O,eff} = \varepsilon^{\tau} D_{H_2O} \quad (15)$$

The above governing equations can be deduced to dimensionless forms of using proper non-dimensional parameters in Table 1. Note that according to the results obtained by using the order-of-magnitude analysis [17], the Stanton number of a typical diffusion layer is about 1.

2.2. Boundary conditions

The boundary conditions for of the present computational domain are summarized as follows:

(1) At the module inlet,

$$P = P_{in}, \qquad \theta_f = \theta_{f,in}, \qquad \frac{\partial \theta_s}{\partial X} = Bi(\theta_s - \theta_f),$$
$$C_{O_2} = 0.9, \qquad C_{H_2O} = 0.1 \quad (16)$$

The relative humidity of the inlet gases is about 50% RH at the operation temperature of 60 °C.

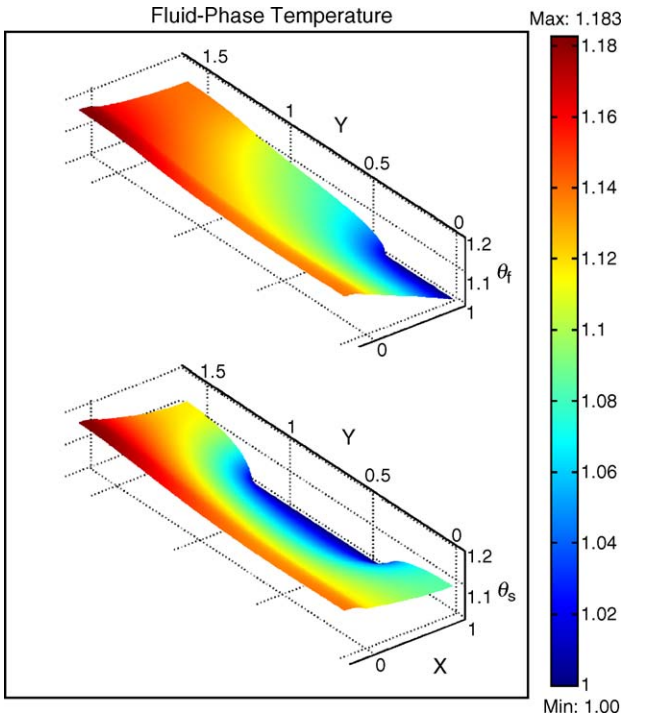

Fig. 3. Comparison of fluid-phase and solid-phase temperature distributions inside the porous electrode for $Re = 6$, $Da = 9.8 \times 10^{-6}$, and $St = 0.74$.

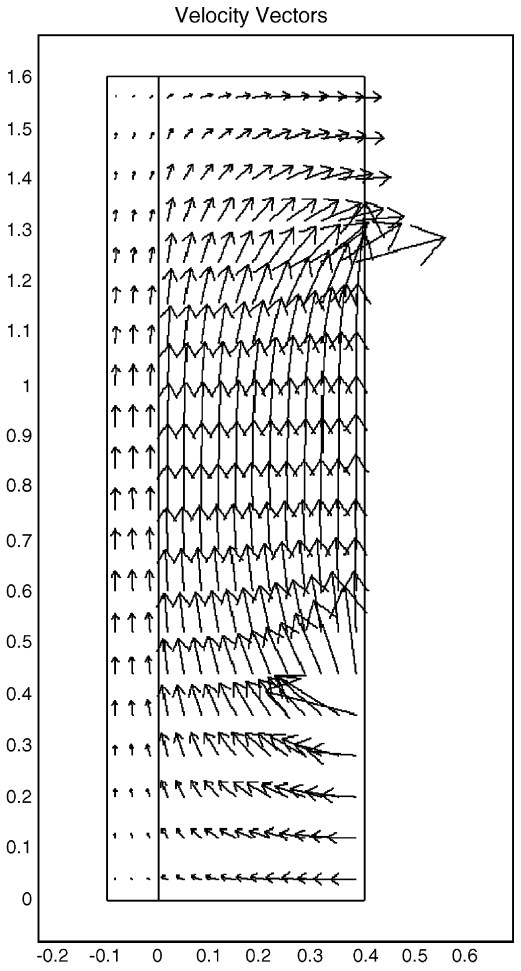

Fig. 2. Velocity distributions inside of porous cathode of a polymer electrolyte fuel cell.

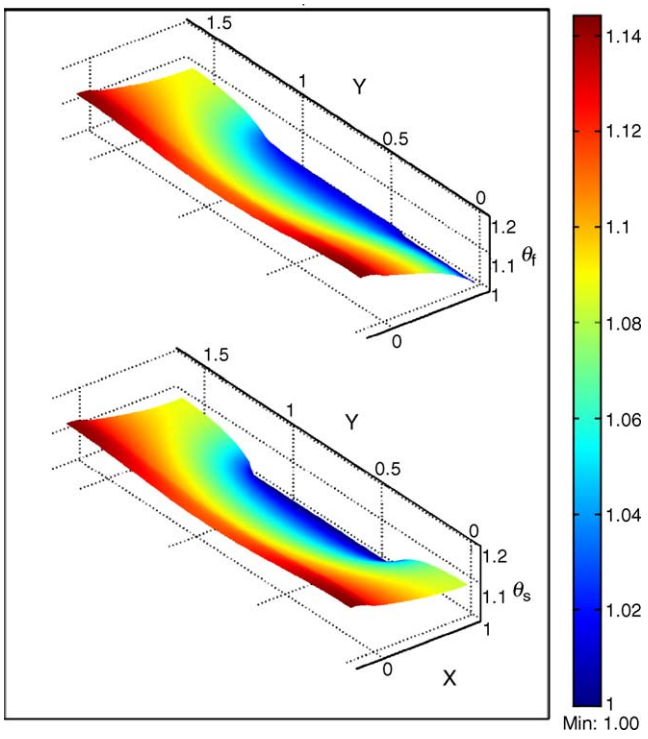

Fig. 4. Comparison of fluid-phase and solid-phase temperature distributions inside the porous electrode for $Re = 6$, $Da = 9.8 \times 10^{-6}$, and $St = 14.73$.

(2) At the rib (current collector) surfaces,

$$\frac{\partial P}{\partial X} = 0, \qquad U = V = 0, \qquad \theta_s = 1,$$
$$\frac{\partial \theta_f}{\partial X} = St(\theta_s - \theta_f), \qquad \frac{\partial C_{O_2}}{\partial X} = \frac{\partial C_{H_2O}}{\partial X} = 0 \tag{17}$$

(3) At the interface of the membrane and the catalyst layer ($X = -0.1$),

$$U = V = 0,$$
$$\frac{\partial P}{\partial X} = \frac{\partial \theta_s}{\partial X} = \frac{\partial \theta_f}{\partial X} = \frac{\partial C_{O_2}}{\partial X} = \frac{\partial C_{H_2O}}{\partial X} = 0 \tag{18}$$

(4) At the symmetric planes,

$$\frac{\partial P}{\partial Y} = \frac{\partial U}{\partial Y} = \frac{\partial V}{\partial Y} = \frac{\partial \theta_s}{\partial Y} = \frac{\partial \theta_f}{\partial Y} = \frac{\partial C_{O_2}}{\partial Y} = \frac{\partial C_{H_2O}}{\partial Y} = 0 \tag{19}$$

(5) At the module outlet,

$$P = P_{out}, \qquad \frac{\partial \theta_f}{\partial X} = 0, \qquad \frac{\partial \theta_s}{\partial X} = Bi(\theta_s - \theta_f),$$
$$\frac{\partial C_{O_2}}{\partial X} = \frac{\partial C_{H_2O}}{\partial X} = 0 \tag{20}$$

2.3. Numerical approaches

The governing equations are numerically solved by the finite-element method. It uses the Broyden's method with an LU-decomposition pre-conditioner to solve the nonlinear equations iteratively. A penalty term is employed for pressure to reduce continuity errors. Thus, there is a continuous part of the pressure and piecewise constant part providing and extra DOF (degree of freedom) for pressure on each element. It uses Newton–Raphson iteration to solve the close-coupled groups (velocity, pressure, temperature, concentration and electricity) and uses the frontal algorithm (Gaussian elimination) to solve the linearized system of equations for each iteration. Variable grids in the x-direction and uniform grids in the y-direction were employed in the present study. Solutions are considered to be converged when all residual sources (including mass, momentum, temperature, species and charge) were less than 1.0×10^{-6}. A typical simulation requires about 60 min of central processing unit time on a Pentium IV 2.80 GHz PC.

3. Results and discussion

3.1. Velocity distributions

Fig. 2 shows the distribution of flow velocity vectors in the porous electrode. The Reynolds number and Darcy number are fixed at $Re = 12$ and $Da = 9.8 \times 10^{-6}$, respectively. It is seen that the velocities are higher in the diffusion layer than in the catalyst layer. This is because the diffusion layer accompanies a higher porosity and a higher permeability. In addition, the velocities near the shoulder surface are higher as compared to those adjacent to the catalyst layer. This is reasonable because the flow paths from the inlet channel to the outlet channel are shorter for the flow closer to the shoulder surface. A shorter flow path has a lower pressure-drop penalty, which allows more fluids to pass through (Table 2).

3.2. Porous matrix temperatures

Figs. 3–5 compare the distributions of the fluid-phase temperature (θ_f) and the solid-phase temperature (θ_s) in the porous cathode under various Stanton numbers. The Reynolds number and Darcy number are fixed at $Re = 12$, and $Da = 9.8 \times 10^{-6}$, respectively.

A low fluid-phase temperature from the module inlet ($X = 1.0$) increases as the flow approaches the catalyst layer ($X = 0$) and then moves downstream. In contrast, the solid-phase temperature decreases along X-direction from the catalyst layer to the rib-shoulder surfaces. Near the module inlet, the hot solid matrices transfer a part of heat to the cold fluids via convection. Around the rib shoulder, the fluid-phase temperatures are higher than the solid-phase ones. This indicates that the heat possessed with the high-temperature fluids not only is carried downstream by bulk motion but is also convected to the solid matrices, and is then conducted out through the rib-shoulder surfaces. When the Stanton number increases to $St = 14.73$, as show in Fig. 4, the temperature discrepancy between the solid and fluid phases is less significant. It means that the porous medium approaches the local thermal equilibrium. As the Stanton number further increases to $St = 1.47 \times 10^3$, as shown in Fig. 5, the distributions of the fluid-phase and solid-phase temperatures are almost

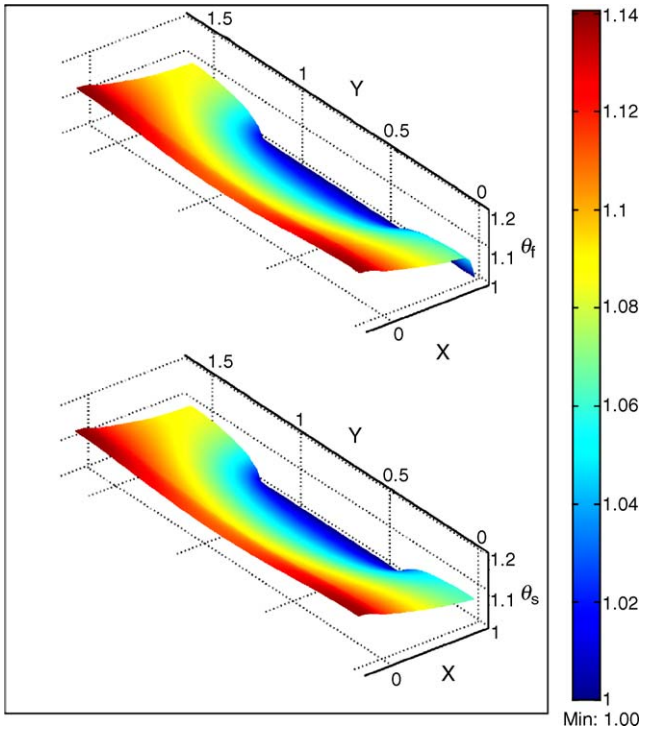

Fig. 5. Comparison of fluid-phase and solid-phase temperature distributions inside the porous electrode for $Re = 6$, $Da = 9.8 \times 10^{-6}$, and $St = 1.47 \times 10^3$.

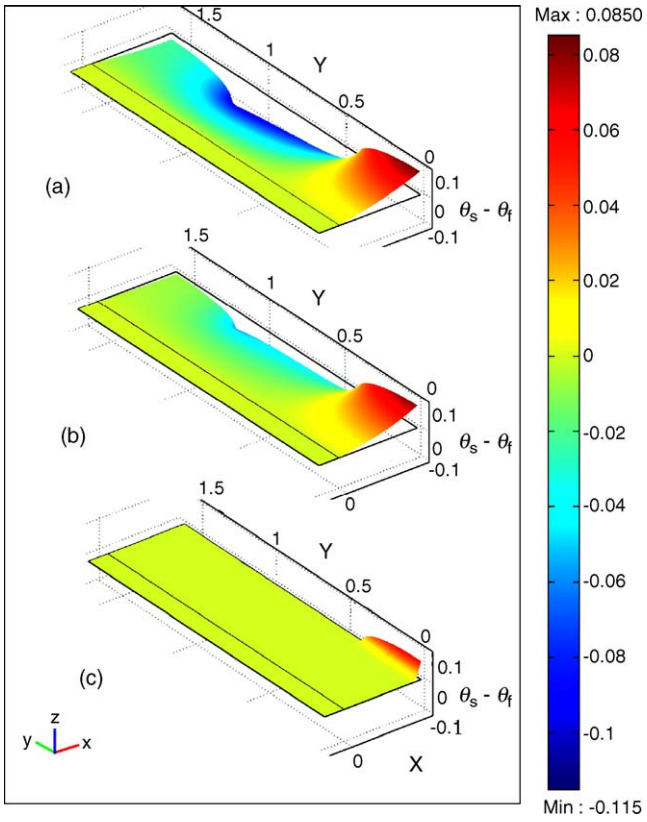

Fig. 6. Effect of heat transfer coefficient on the temperature difference between the solid phase and fluid phase: (a) $h_V = 5.0 \times 10^5$; (b) $h_V = 2.0 \times 10^6$, and (c) $h_V = 1.0 \times 10^9$ W m^{-3} K.

the same, except for the region near the module inlet ($Y = 0.5$, $0.9 < X < 1.0$). A large similarity in the temperature distribution between the solid matrices and the fluids gives an indication that the thermal-fluid field in the porous electrode has become local thermal equilibrium.

Fig. 6 further shows the effect of h_V (5.0×10^5, 2.0×10^6, and 1.0×10^9 W m^{-3} K^{-1}) on the temperature difference between the solid matrices and the reactant fluids. Clearly, the solid matrices and reactant fluid have the same temperatures in the catalyst layer ($-0.25 < X < 0$). In the diffusion layer ($0 < X < 1.0$), however, the temperatures between the reactant fluids and the carbon fibers are different. At the module inlet, the fluid-phase temperature is lower than that of the solid-phase. In contrast, the solid-phase temperature is lower than the fluid-phase one near the rib shoulder. The maximum temperature difference is about -0115 for $h_V = 5.0 \times 10^5$ W m^{-3} K^{-1}. It decreases with increasing the heat transfer coefficient.

3.3. Heat fluxes

Fig. 7 shows the heat flux distributions along the $X = 0.4$ through which all heat should be removed convectively by fluid (Q_f) or conducted out by solid (Q_s). The non-dimensional heat flux through the solid and fluid phases on the reaction surfaces can be represented by $Q_s = -(\partial\theta_s/\partial X)_w$ and $Q_f = -R_k(\partial\theta_f/\partial X)_w$, respectively. It is seen that the heat transfer by

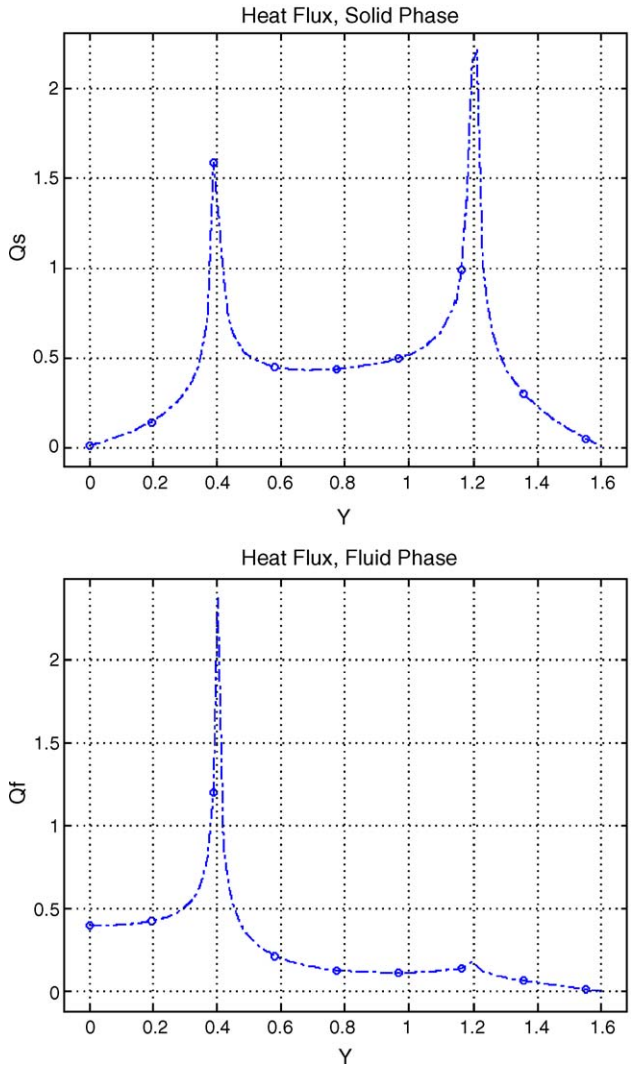

Fig. 7. Heat flux distributions along the $X = 1.0$ for $Da = 9.8 \times 10^{-6}$, and $Re = 12$.

the solid-phase conduction is higher than that by the fluid phase. This is because the significantly higher thermal conductivity of the solid phase (Table 1) can provide a wider thermal pathway for channelling out the heat.

3.4. Species fluxes

The oxygen fluxes and the water-vapour fluxes in the porous cathode are shown as vectors in Figs. 8 and 9, respectively. The total species fluxes can be decomposed into two parts, i.e., convective fluxes and diffusive fluxes. As shown in Fig. 8(a), the vectors of oxygen convective fluxes direct from the module entrance toward the module outlet, which are similar to those of the velocity. As for the oxygen diffusive fluxes (Fig. 8(b)), the vectors direct from the module entrance toward the catalyst layer and decrease in magnitude gradually. This is because the oxygen is consumed by the electrochemical reaction in the catalyst layer. It is noted that the oxygen diffusive fluxes are larger than the oxygen convective fluxes. The water-vapour vectors

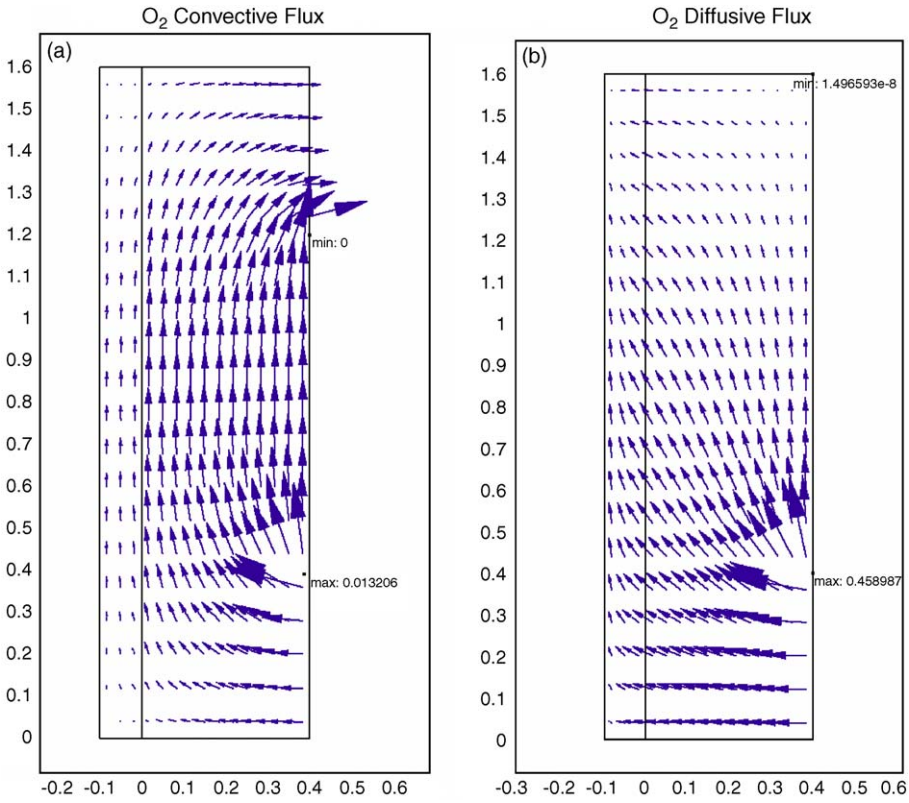

Fig. 8. Comparison of convective and diffusive species fluxes of oxygen in the porous cathode of a polymer electrolyte fuel cell: (a) convective fluxes; (b) diffusive fluxes.

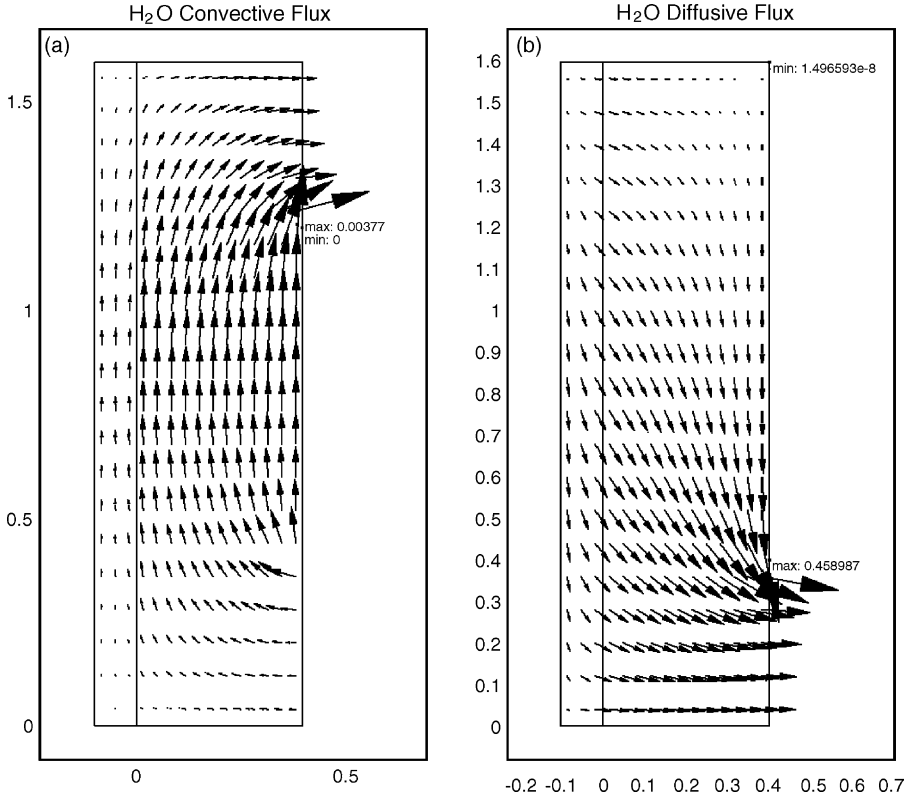

Fig. 9. Comparison of convective and diffusive species fluxes of water vapour in the porous cathode of a polymer electrolyte fuel cell: (a) convective fluxes; (b) diffusive fluxes.

of convective fluxes (Fig. 9(a)) are largely similar to those of the oxygen convective fluxes (Fig. 8(a)). The water vapours are produced by the electrochemical reaction in the catalyst layer, and thus direct their fluxes diffusively from the catalyst layer toward the module entrance. Again, the water-vapour diffusive fluxes are significantly larger than the water-vapour convective fluxes.

4. Conclusions

Detailed phase-temperature distributions inside a porous cathode of a polymer electrolyte fuel cell in contact with a typical interdigitated flow field have been studied numerically. The thermal interaction between the solid matrices and the reactant fluid in the porous electrode of a polymer electrolyte fuel cell is discussed in detail by examining the effect of the intrinsic heat transfer coefficient. A two-equation local thermal non-equilibrium model is implemented to investigate the heat transfer into the fuel cell porous cathode. In species transports, the Bruggemann model is employed to describe the effective diffusivities of the oxygen and water vapour in the porous electrode.

Results show that the wall temperature decreases with increasing the intrinsic heat transfer coefficient. The local maximum wall temperature always occurs at the downstream end of the module. As the intrinsic heat transfer coefficients increase, the porous electrode becomes local thermal equilibrium with a strong thermal interaction (heat transfer) between the solid and fluid phases. Under the conditions of high intrinsic heat transfer coefficients, the temperature difference between the solid matrices and the reactant fluids are negligible.

Acknowledgement

This work was partly sponsored by the National Science Council of the Taiwan, ROC under contract no. NSC 92-2212-E-451-002.

References

[1] J. Yuan, M. Rokni, B. Sunden, Int. J. Heat Mass Transfer 46 (2003) 809–821.
[2] J.S. Yi, T.V. Nguyen, J. Electrochem. Soc. 145 (1998) 1149–1159.
[3] T. Berning, D.M. Lu, N. Djilali, J. Power Sources 106 (2002) 284–294.
[4] J.J. Hwang, C.K. Chen, R.F. Savinell, C.C. Liu, J. Wainright, J. Appl. Electrochem. 34 (2004) 217–224.
[5] V. Gurau, H. Liu, S. Kakac, AIChE J. 44 (1998) 2410–2422.
[6] D.M. Bernardi, M.W. Verbrugge, Am. Inst. Chem. Eng. J. 37 (1991) 1151–1163.
[7] T.E. Springer, T.A. Zawodzinski, S. Gottesfeld, J. Electrochem. Soc. 138 (1991) 2334–2342.
[8] T.V. Nguyen, R.E. White, J. Electrochem. Soc. 140 (1993) 2178–2186.
[9] N. Djilali, D.M. Lu, Int. J. Therm. Sci. 41 (2002) 29–40.
[10] M. Quintard, S. Whitaker, Theoretical modeling of transport in porous media, in: K. Vafai (Ed.), Handbook of Heat Transfer in Porous Media, 1st ed., M. Decker, New York, 2000.
[11] M. Kaviany, Principles of Heat Transfer in Porous Media, 2nd ed., Springer, Berlin, 1995.
[12] J.J. Hwang, G.J. Hwang, R.H. Yeh, C.H. Chao, ASME J. Heat Transfer 124 (2002) 120–129.
[13] J.J. Hwang, W.Y. Ho, C.L. Chang, D.Y. Wang, J. Power Sources (in press).
[14] J.J. Hwang, J. Electrochem. Soc. 153 (2006) A216–A224.
[15] H. Oldham, J. Myland, Fundamentals of Electrochemical Science, Academic Press Inc., 1994.
[16] J.J. Hwang, P.Y. Chen, Int. J. Heat Mass Transfer (in press).
[17] J.J. Hwang, C.K. Chen, D.Y. Lai, J. Power Sources 140 (2005) 235–242.